

The VLA-COSMOS Survey. V. 324 MHz continuum observations

Vernesa Smolčić^{1*}, Paolo Ciliegi², Vibor Jelić^{3,4}, Marco Bondi⁵, Eva Schinnerer⁶,
Chris L. Carilli⁷, Dominik A. Riechers⁸, Mara Salvato⁹, Alen Brković¹⁰,
Peter Capak¹¹, Olivier Ilbert¹², Alexander Karim¹³, Henry McCracken¹⁴, Nick Z. Scoville¹⁵

¹University of Zagreb, Physics Department, Bijenička cesta 32, 10002 Zagreb, Croatia

²INAF-Osservatorio Astronomico di Bologna, Via Ranzani 1, I - 40127 Bologna, Italy

³Kapteyn Astronomical Institute, University of Groningen, PO Box 800, 9700 AV Groningen, the Netherlands

⁴ASTRON - the Netherlands Institute for Radio Astronomy, PO Box 2, 7990 AA Dwingeloo, the Netherlands

⁵Istituto di Radioastronomia di Bologna - INAF, via P. Gobetti, 101, 40129, Bologna, Italy

⁶Max-Planck-Institut für Astronomie, Königstuhl 17, D-69117 Heidelberg, Germany

⁷National Radio Astronomy Observatory, P.O. Box 0, Socorro, NM 87801, USA

⁸Department of Astronomy, Cornell University, Ithaca, New York 14853, USA

⁹Max-Planck-Institut für extraterrestrische Physik, Garching bei München, Germany

¹⁰University of Dubrovnik, Branitelja Dubrovnika 29, 20000 Dubrovnik, Croatia

¹¹Spitzer Science Center, 314-6 Caltech, Pasadena, CA 91125, USA

¹²Aix Marseille Universit, CNRS, LAM (Laboratoire d'Astrophysique de Marseille), UMR 7326, 13388, Marseille, France

¹³Argelander-Institute for Astronomy, Auf dem Hugel 71, 53121 Bonn, Germany

¹⁴Institut d'Astrophysique de Paris, UMR7095 CNRS, Universit Pierre et Marie Curie, 98 bis Boulevard Arago, 75014, Paris

¹⁵California Institute of Technology, MC 249-17, 1200 East California Boulevard, Pasadena, CA 91125, USA

21 July 2014

ABSTRACT

We present 90 cm VLA imaging of the COSMOS field, comprising a circular area of 3.14 square degrees at $8.0'' \times 6.0''$ angular resolution with an average rms of 0.5 mJy/beam. The extracted catalog contains 182 sources (down to 5.5σ), 30 of which are multi-component sources. Using Monte Carlo artificial source simulations we derive the completeness of the catalog, and we show that our 90 cm source counts agree very well with those from previous studies. Using X-ray, NUV-NIR and radio COSMOS data to investigate the population mix of our 90 cm radio sample, we find that our sample is dominated by active galactic nuclei (AGN). The average 90-20 cm spectral index ($S_\nu \propto \nu^\alpha$, where S_ν is the flux density at frequency ν , and α the spectral index) of our 90 cm selected sources is -0.70, with an interquartile range of -0.90 to -0.53. Only a few ultra-steep-spectrum sources are present in our sample, consistent with results in the literature for similar fields. Our data do not show clear steepening of the spectral index with redshift. Nevertheless, our sample suggests that sources with spectral indices steeper than -1 all lie at $z \gtrsim 1$, in agreement with the idea that ultra-steep-spectrum radio sources may trace intermediate-redshift galaxies ($z \gtrsim 1$).

Key words: surveys; galaxies: clusters: general, active; radiation mechanisms: general; radio continuum: galaxies; X-rays: galaxies: clusters

1 INTRODUCTION

In the last decades optical sky surveys have proven as optimum tools to study properties of galaxies, their formation and evolution. The radio regime is important in this context as the observed synchrotron emission from galaxies traces dust-unbiased star formation and active galactic nuclei (AGN). It traces both

the high-excitation radio AGN¹ that follow the Unified model for AGN, and low-excitation radio AGN, not identified as AGN at any other observing wavelength, and inconsistent with the Unified model for AGN (e.g. Ho 2005; Hardcastle, Evans & Croston 2007; Evans et al. 2006; Smolčić 2009). The radio AGN types exhibit systematic differences in their physical properties; low-excitation radio AGN are hosted by red sequence galaxies with the highest

* E-mail: vs@phy.hr

¹ High-excitation AGN are defined as those with high-excitation emission lines in their optical spectra, while the spectra of low-excitation AGN are devoid of such lines (Hine & Longair 1979).

stellar and central supermassive black hole masses, yet the accretion onto their black holes is at sub-Eddington levels (Evans et al. 2006; Smolčić 2009; Best & Heckman 2012). They are thought to be the population postulated in cosmological models responsible for exerting radio-mode AGN feedback, a heating ingredient in the models necessary to reproduce observed galaxy properties, such as the masses of red galaxies (Croton et al. 2006; Bower et al. 2006; Sijacki & Springel 2006). On the other hand, high-excitation radio AGN are hosted by intermediate mass, 'green valley' galaxies, with intermediate mass supermassive black holes accreting at Eddington levels (e.g. Ho 2005; Hardcastle, Evans & Croston 2007; Evans et al. 2006; Smolčić 2009).

Although several radio surveys have been obtained at low radio frequencies (Bondi et al. 2007; Tasse et al. 2007; Owen et al. 2009; Sirothia et al. 2009), to-date the majority of radio surveys have been conducted at 1.4 GHz (20 cm). Opening a new frequency window at lower frequencies offers several advantages, such as detailed radio synchrotron spectral index assessment allowing more precise determination of galaxies' physical properties (e.g. Jelić et al. 2012), their cosmic evolution (e.g. Smolčić et al. 2009) and direct identification of intermediate-redshift ($z \gtrsim 1$) radio sources via ultra-steep synchrotron spectra (e.g. De Breuck et al. 2002). Compared to frequencies ≥ 1.4 GHz, synchrotron emission at lower frequencies is less affected by synchrotron losses with time (proportional to the square of the frequency), and it has been shown to better correlate with the mechanical power output of radio galaxies into their environment (Bîrzan et al. 2004, 2008), a crucial aspect for studies of radio-mode AGN feedback. Moreover, compared with other information, the low frequency spectral energy distribution can be used to study the physics of AGN and star-forming galaxies (e.g. Bîrzan et al. 2004, 2008; Oklopčić et al. 2010; Jelić et al. 2012).

Analyzing their 90 cm data down to a 5σ flux limit of 0.35 mJy in the SWIRE *Spitzer* legacy field, Owen et al. (2009) found a mean spectral index of -0.7 , few very steep spectrum sources implying the absence of a large population of very steep (and high redshift) radio sources to the limit of their survey and a flattening of the 90 cm source counts below 3-5 mJy, respectively. A similar flattening of the 90 cm source counts has been found also by Sirothia et al. (2009) in the ELAIS N1 field. This flattening in the radio source counts has been reported earlier at higher frequencies and attributed to both starburst galaxies and low luminosity AGN (e.g. Smolčić et al. 2008).

Here we present 324 MHz (90 cm) continuum observations of the COSMOS field with the Very Large Array. These low frequency radio data complement the existing 1.4, and ongoing 3 GHz coverage of the COSMOS field at radio wavelengths (Schinnerer et al. 2004, 2007, 2010, Smolčić et al., in prep.) providing one of the best fields studied in the radio range and an ideal laboratory for the next generation radio facilities like ASKAP (Johnston et al. 2007), EMU (Norris et al. 2011) and the Square Kilometer Array (SKA). To date the COSMOS field has been observed with most major space- and ground-based telescopes over nearly the full electromagnetic spectrum reaching high sensitivities (Scoville et al. 2007; Capak et al. 2007; Schinnerer et al. 2007; Taniguchi et al. 2007; Mobasher et al. 2007; Trump et al. 2007; Lilly et al. 2007, 2009; Hasinger et al. 2007; Elvis et al. 2009; Koekemoer et al. 2007; Sanders et al. 2007; McCracken et al. 2012).

In Sec. 2 we describe the observations and data reduction while in Sec. 3 and Sec. 4 we describe the construction of the catalog and the 90 cm source counts. A multiwavelength analysis is reported in Sec. 5, while our conclusions are summarized in Sec. 6.

We define the radio synchrotron spectrum as $S_\nu \propto \nu^\alpha$ where S_ν is the radio flux density at frequency ν , and α is the spectral index.

2 OBSERVATIONS, DATA REDUCTION AND IMAGING

Observations were performed in November 2008 with the VLA in its A configuration. The receivers were tuned to 324 MHz (90 cm, P-band). A single pointing towards the COSMOS field (centered at 10:00:28.6, +02:12:21) was targeted, resulting in a primary beam diameter (FWHM) of 2.3° , and a resolution of $8.0'' \times 6.0''$ in the final map. A total of 24 hours of observations were scheduled during three nights. Due to the upgrade of some VLA antennas, and the incompatibility of the P-band receivers with the upgrade, about half of the data was lost, implying a total integration time of ~ 12 hrs for a 27 antenna array.

The data were taken in spectral line mode to minimize bandwidth smearing. Two intermediate frequencies (IFs, each with two polarizations) were centered at 321.56 and 326.56 MHz, respectively (we hereafter take the average frequency of 324.1 MHz as the representative one). A total bandwidth of 3.027 MHz per IF was observed using 31 channels of 97.66 kHz bandwidth each, resulting in a final bandwidth of 6.027 MHz. The source J0521+166 (3C 138), observed at the beginning of each observing run for ~ 13 minutes, was used for flux and bandpass calibration. The source J1024-008, observed for 1.5 minutes every ~ 40 minutes between target observations, was used for phase and amplitude calibration. The data reduction was done in AIPS (Greisen 1990). Bad data were flagged manually (using the AIPS task TVFLG) in each channel before, as well as after calibration to reduce radio frequency interference that could downgrade the quality of the final map.

After data calibration, the two IFs and two polarizations were imaged separately using a cell size of $1.7'' \times 1.7''$ (which appropriately samples the CLEAN beam of $8'' \times 6''$), and 61 separate facets of the field (using the AIPS task SETFC). Twenty more facets were generated using the NVSS catalog to account for bright sources outside the field as these could cause strong side-lobes in the field of interest. The facets were deconvolved via the CLEAN algorithm using the AIPS task IMAGR. CLEAN boxes were set manually around sources. The combined image of the two IFs and two polarizations was then used as the input model for self-calibration of the data in order to improve the image quality and further reduce the rms in the map. Self-calibration and imaging as described above were performed multiple times in an iterative manner until satisfactory results were reached. The final imaging was performed on the two IFs and two polarizations separately using ROBUST=0. The 4 maps were then combined into the final map which was corrected for the primary beam response (using the AIPS task PBCOR with a cut-off at 70% response limiting the mapped area to ~ 3.14 square degrees). The final map, shown in Fig. 1, reaches an angular resolution of $8.0'' \times 6.0''$ and has an average rms of ~ 0.5 mJy/beam.

3 THE 90 CM SOURCE CATALOG: CONSTRUCTION AND COMPLETENESS

3.1 Component Extraction: Search and Destroy at 90 cm

The whole image shown in Fig. 1 (a circular area of radius 1 degree) has been used to identify 90 cm radio components. In order to select a sample of sources above a given threshold, defined in terms

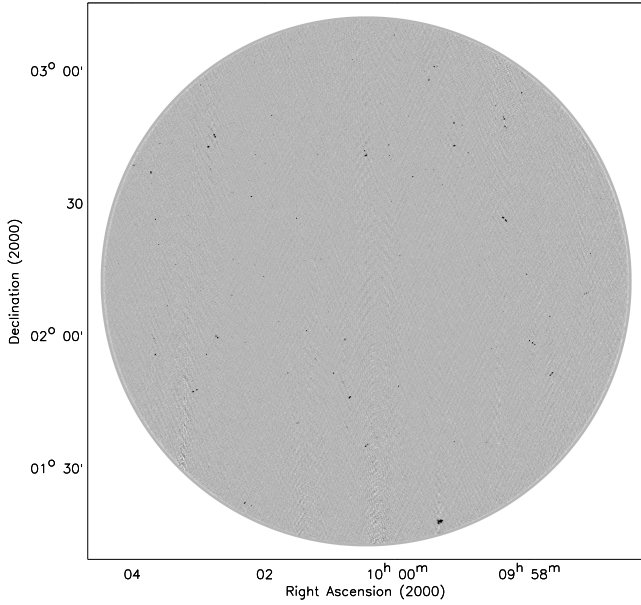


Figure 1. COSMOS field observed at 90 cm.

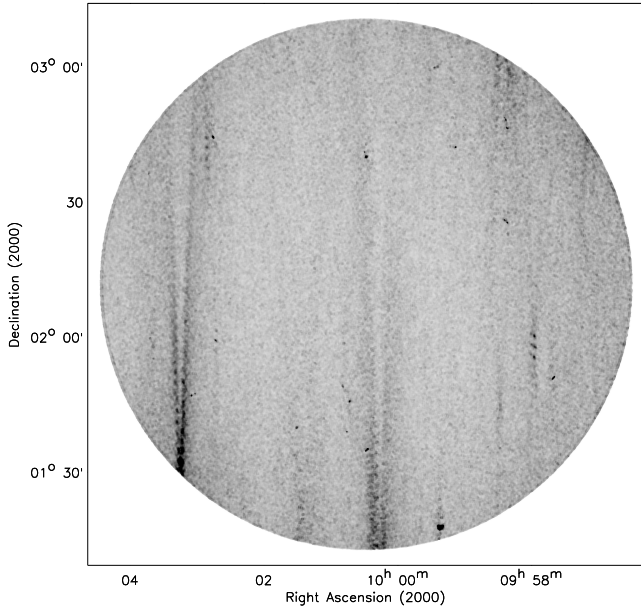


Figure 2. The noise map of the 324 MHz COSMOS field derived via AIPS/RMSD task with a mesh size of 20 pixels.

of local signal-to-noise ratio, we adopted the approach already successfully tested during the extraction of the VLA-COSMOS 20 cm sources (Schinnerer et al. 2007). First, the AIPS task RMSD was used to estimate the local background using a mesh size of 20 pixels, corresponding to $34''$. The resulting rms map is shown in Fig. 2 while the distribution of the local rms value is shown in Fig. 3. The rms values range from about 0.30 mJy/beam in the inner regions to about 0.50-0.60 mJy/beam at the edge of the map, with values as high as 1-2 mJy/beam in the strong side-lobes present in the map. The mean rms of the full map is 0.51 mJy/beam with a mode value of 0.46 mJy/beam. The cumulative area, as a function of rms is shown in Fig. 4.

Using both the signal and rms maps (Fig. 1 and Fig. 2) as in-

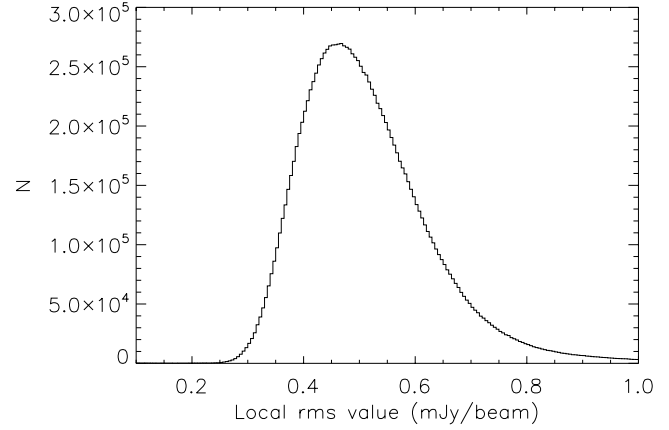


Figure 3. Distribution of the local rms value. The positive tail is due to sources and to strong side lobes present in the map (see Fig. 2).

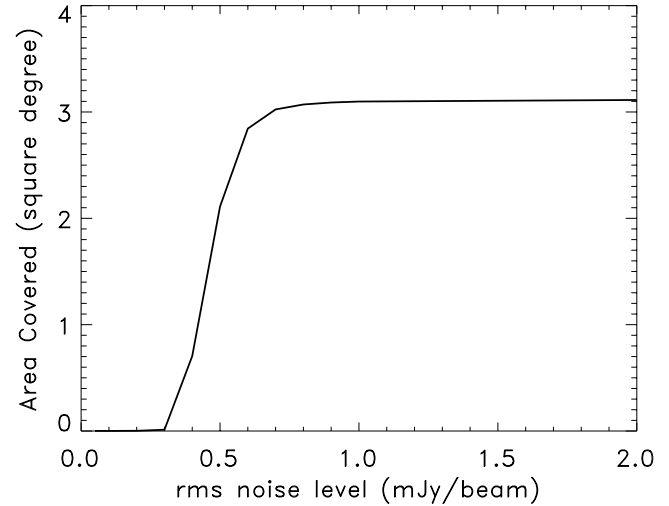


Figure 4. Plot of the rms noise level vs. cumulative area covered. The full area covered is ~ 3.14 square degrees.

put data we ran the AIPS task SAD to obtain a catalog of candidate components above a given local signal-to-noise ratio threshold. The task SAD was run four times with search levels of 10, 8, 6 and 5 in signal-to-noise ratio, using the resulting residual image each time. We recovered all the radio components with a local signal-to-noise ratio greater than 5.00. Subsequently, all the selected components have been visually inspected, in order to check their reliability, especially for the components near strong side-lobes. After a careful analysis, a signal-to-noise ratio threshold of 5.50 has been adopted as the best compromise between a deep and a reliable catalog. The procedure yielded a total of 246 components with a local signal-to-noise ratio greater than 5.50.

3.2 Source identification, source sizes and catalog

More than one component, identified in the 90 cm map as described in the previous section, sometimes belongs to a single radio source (e.g. large radio galaxies consist of multiple components). Using the 90 cm COSMOS radio map we have combined the various components into single sources based on visual inspection. The final catalog lists 182 radio sources, 30 of which have been classified as multiple, i.e. they are better described by more than a single com-

ponent. Moreover, in order to ensure a more precise classification, all sources identified as multi-component sources have been also double-checked using the 20 cm radio map. We found that all the 26 multiple 90 cm radio sources within the 20 cm map have 20 cm sources already classified as multiple.

To generate our final 90 cm source catalog we make use of the VLA-COSMOS Large and Deep Projects over 2 square degrees, reaching down to an rms of $\sim 15 \mu\text{Jy/beam}$ at 1.4 GHz and $1.5''$ resolution (Schinnerer et al. 2007). The 90 cm COSMOS radio catalog has, however, been extracted from a region of 3.14 square degrees (see Fig. 1 and Sec. 3.1). This implies that a certain number of 90 cm sources (48) lie outside the area of the 20 cm COSMOS map used to select the radio catalog. Thus, to identify the 20 cm counterparts of the 90 cm radio sources, we used the joint VLA-COSMOS catalog (Schinnerer et al. 2010) for the 134 sources within the 20 cm VLA COSMOS area and the VLA - FIRST survey (White et al. 1997) for the remaining 48 sources. The 90 cm sources were cross-matched with the 20 cm VLA-COSMOS sources using a search radius of 2.5 arcsec, while the cross-match with the VLA-FIRST sources has been done using a search radius of 4 arcsec in order to take into account the larger synthesized beam of the VLA - FIRST survey (~ 5 arcsec). Finally, all the 90 cm-20 cm associations have been visually inspected in order to ensure also the association of the multiple 90 cm radio sources for which the value of the search radius used during the cross-match could be too restrictive. In summary, out of the total of 182 sources in our 90 cm catalog, 168 have counterparts at 20 cm.

In our 90 cm catalog multiple component sources are identified by the flag "Mult=1". Since the radio core of these multiple sources is not always detected, following the same procedure adopted for the 20 cm catalogue, their *virtual* radio position has been calculated as the mean value of the position of all components weighted for their total radio flux. Moreover, in order to avoid slightly different *virtual* positions, for the 26 multiple 90 cm sources that have been visually associated to a 20 cm multiple source (see above) the position has been assumed to be coincident with the 20 cm position. For all the multiple sources, the total flux was calculated using the AIPS task TVSTAT, which allows the integration of the map values over irregular areas. For these sources the peak flux (at the listed position) is undetermined and therefore set to a value of -99.999. Finally, for all the 90 cm single component sources, we report the position estimated on the 90 cm map, even for those with a 20 cm counterpart.

In order to determine whether our identified single-component sources are resolved (i.e. extended, larger than the clean beam) we make use of the ratio between total (S_T) and peak (S_P) fluxes (both calculated with the AIPS Gaussian fitting algorithm JMFIT within AIPS/SAD) as this is a direct measure of the extension of a radio source (see Bondi et al. (2003)). In Fig. 5 we plot the ratio between the total and the peak flux density as a function of the signal to noise ratio $S/N (=S_P/\text{rms})$ for all the 152 single component sources in the catalog. To select the resolved sources, we determined the lower envelope of the points in Fig. 5, which contains 90% of the sources with $S_T < S_P$ and mirrored it above the $S_T/S_P=1$ line (upper envelope in Fig. 5). We consider the 56 sources lying above the upper envelope resolved which in addition to the 30 multi component sources gives a total of 86 resolved sources. The upper envelope of Fig. 5 can be characterized by the equation $S_T/S_P=1+[100/(S_P/\text{rms})]^{2.35}$. The resolved sources are flagged in the catalog by "Res=1". For the unresolved sources the total flux density is set equal to the peak brightness and the angular size is undetermined and set equal to zero in the catalog.

Finally, following the procedure adopted for the VLA COSMOS 20 cm survey, the uncertainties in the peak flux density S_P and integrated flux S_T have been calculated using the equation given by Condon (1997, see also Hopkins et al. 2003; Schinnerer et al. 2004). For the positional uncertainties we used the equations reported in Bondi et al. (2003) (their eqs. [4] and [5]).

Following Condon (1997), calibration terms must be estimated from comparison with external data with better accuracy than the one tested. This is best done using sources strong enough (high S/N), thus yielding the noise terms in equation 4 and 5 much smaller than the calibration terms. Our calibration terms have been calculated from the comparison between the position of single component VLA COSMOS 90 cm sources with $S/N > 10$ and the position of the VLA COSMOS 20 cm counterpart (68 in total). The mean values and standard deviations found from this comparison are $\langle \text{RA} \rangle = 0.22 \pm 0.32$ arc sec and $\langle \text{DEC} \rangle = -0.27 \pm 0.39$ arcsec. These values are consistent with no systematic offset in right ascension and declination and with a calibration term of 0.3 arcsec in RA and 0.4 arcsec in DEC.

A sample page of the catalog is shown in Tab. 1. For each source we report the 90 cm name, the RA and DEC position, the error on the position (σ_{RA} and σ_{DEC}), the peak flux with relative error, the total flux with relative error, the 90 cm rms calculated on the position of the source, the deconvolved size of major and minor axes (θ_M and θ_m) and positional angle (PA) for resolved sources, the flag for resolved (Res = 1) and unresolved (Res = 0) sources, the flag for multiple (Mult = 1) or single (Mult = 0) component sources, the name of the 20 cm counterpart, the 20 cm peak flux, the 20 cm total flux, and the separation between the 90 and 20 cm positions. The full catalog is available in electronic format at the COSMOS IRSA archive.

3.3 Comparison with the 20 cm VLA-COSMOS data: 90 cm – 20 cm spectral indices

The distribution of the 90-20 cm spectral indices is shown in Fig. 6. We find a median value of -0.70 with an interquartile range of -0.90 to -0.53 , consistent with the values typically found for radio sources at these flux levels (e.g. Kimball & Ivezić 2008; Owen et al. 2009), and further confirming the validity of our 90 cm fluxes.

Fourteen COSMOS 90 cm radio sources do not have a 20 cm counterpart (six of which lie within the 20 cm COSMOS area). The distribution of their 90-20 cm spectral indices, computed using the VLA-COSMOS and FIRST source detection limits of $75 \mu\text{Jy}$ and 1 mJy , respectively, is also shown in Fig. 6. As expected given the non-detections at 20 cm, these sources have spectral indices steeper than $\alpha \sim -1$. They could be ultra-steep spectrum sources, often located at high redshifts (see Sec. 5.3 and Fig. 11). However, we cannot exclude the possibility that some of them may also be spurious, specially the seven sources with a relatively low S/N (< 6.5).

3.4 Survey Completeness Tests

In order to estimate the combined effect of noise, source extraction and flux determination on the completeness of our sample, following the method described in Bondi et al. (2003) we constructed simulated samples of radio sources down to a flux level of 0.9 mJy , i.e. more than a factor of 3 lower than the minimum flux we used to derive the source counts (see next section). This allows us to account for those sources with an intrinsic flux below the detection

Table 1: 90 cm COSMOS Source Catalog : Sample page

Name	R.A. (J200.0)	Decl (J2000.0)	σ_{RA}	σ_{DEC}	$S_{peak\ 90cm}$	$S_{total\ 90cm}$	rms	θ_M	θ_m	PA	Res	Mult	20 cm Name	S_{peak} (20cm) (mJy/beam)	S_{total} (20cm) (mJy)	20-90cm sep (")
COSMOSVLA327_	(hh:mm:ss.sss)	(dd:mm:ss.sss)	(")	(")	(mJy/beam)	(mJy)	(mJy/beam)	(")	(")	($^{\circ}$)						
095647.05+020745.9	09 56 47.048	02 07 45.861	0.30	0.40	3.88 ± 0.563	3.88 ± 0.563	0.628	0.00	0.00	0.00	0	0	FIRST_VLA_J095646.93+020746.1	2.35	1.63	1.70
095649.58+015601.7	09 56 49.580	01 56 01.671	0.30	0.40	7.16 ± 0.609	9.09 ± 0.774	0.562	4.66	2.48	29.40	1	0	FIRST_VLA_J095649.57+015602.0	4.10	4.38	0.34
095655.60+015951.5	09 56 55.599	01 59 51.498	0.60	0.66	3.60 ± 0.543	3.60 ± 0.543	0.567	0.00	0.00	0.00	0	0	FIRST_VLA_J095655.58+015952.1	1.13	1.22	0.68
095705.55+021840.9	09 57 05.550	02 18 40.885	0.30	0.40	30.53 ± 0.554	31.98 ± 0.580	0.619	2.16	0.61	149.90	1	0	FIRST_VLA_J095705.49+021841.1	10.09	10.91	0.82
095709.38+020940.3	09 57 09.375	02 09 40.286	−99.0	−99.0	−99.0	68.10	0.609	77.00	17.00	−99.00	1	1	FIRST_VLA_J095709.33+020940.7	19.98	19.92	0.72
095730.59+014919.6	09 57 30.587	01 49 19.629	0.43	0.54	3.07 ± 0.502	3.07 ± 0.502	0.478	0.00	0.00	0.00	0	0	no 20 cm counterpart			
095737.30+024604.1	09 57 37.300	02 46 04.053	0.64	0.69	3.82 ± 0.599	3.82 ± 0.599	0.626	0.00	0.00	0.00	0	0	COSMOSVLADP_J095737.21+024604.7	1.23	1.51	1.50
095738.47+023836.4	09 57 38.472	02 38 36.384	0.30	0.40	7.30 ± 0.681	7.30 ± 0.681	0.628	0.00	0.00	0.00	0	0	COSMOSVLADP_J095738.38+023837.7	2.81	3.20	1.90
095741.11+015122.6	09 57 41.107	01 51 22.580	−99.0	−99.0	−99.00	146.03	1.471	72.00	15.30	−99.00	1	1	COSMOSVLADP_J095741.10+015122.5	−99.00	47.23	0.00
095742.34+020425.7	09 57 42.340	02 04 25.660	0.30	0.40	45.72 ± 0.599	49.35 ± 0.646	0.552	3.34	3.34	168.00	1	0	COSMOSVLADP_J095742.30+020426.0	16.17	19.18	0.70
095746.00+021715.3	09 57 46.005	02 17 15.264	0.31	0.40	6.06 ± 0.571	6.06 ± 0.571	0.529	0.00	0.00	0.00	0	0	COSMOSVLADP_J095745.95+021715.2	3.53	3.91	0.71
095758.04+015825.2	09 57 58.044	01 58 25.250	−99.0	−99.0	−99.0	260.33	1.081	90.10	17.00	−99.00	1	1	COSMOSVLADP_J095758.04+015825.2	−99.00	53.03	0.00
095758.28+015330.1	09 57 58.283	01 53 30.144	0.52	0.58	4.24 ± 0.652	4.24 ± 0.652	0.657	0.00	0.00	0.00	0	0	no 20 cm counterpart			
095803.25+021357.1	09 58 03.253	02 13 57.093	0.30	0.40	55.74 ± 0.654	62.15 ± 0.729	0.624	3.25	1.54	4.00	1	0	COSMOSVLADP_J095803.21+021357.7	22.51	25.12	0.85
095807.71+025502.1	09 58 07.714	02 55 02.086	0.31	0.40	20.57 ± 0.707	59.15 ± 2.032	0.771	15.16	4.34	45.00	1	0	FIRST_VLA_J095807.85+025504.1	5.25	6.79	3.03
095817.97+025733.9	09 58 17.969	02 57 33.891	0.30	0.40	8.87 ± 0.940	8.87 ± 0.940	0.867	0.00	0.00	0.00	0	0	FIRST_VLA_J095817.99+025733.6	3.55	3.47	0.43
095821.70+024628.3	09 58 21.704	02 46 28.332	0.35	0.44	5.23 ± 0.753	5.23 ± 0.753	0.709	0.00	0.00	0.00	0	0	COSMOSVLADP_J095821.65+024628.1	5.22	5.22	0.78
095822.30+024721.3	09 58 22.302	02 47 21.330	−99.0	−99.0	−99.0	88.65	0.982	50.72	17.00	−99.00	1	1	COSMOSVLADP_J095822.30+024721.3	−99.00	30.12	0.00
095822.94+022619.8	09 58 22.936	02 26 19.800	−99.0	−99.0	−99.0	472.14	1.406	96.16	15.30	−99.00	1	1	COSMOSVLADP_J095822.93+022619.8	−99.00	116.50	0.00

Table 2. 90 cm COSMOS simulation results

Flux bin (mJy)	Input	Detected	C (σ_C)
2.00 - 3.00	884	398	2.2 (0.05)
3.00 - 4.50	534	492	1.1 (0.07)
4.50 - 6.75	552	543	1.0 (0.09)
6.75 - 10.13	249	258	1.0 (0.10)
10.13 - 15.19	189	190	1.0 (0.11)
15.19 - 22.78	206	213	1.0 (0.12)
22.78 - 34.17	183	183	1.0 (0.11)
34.17 - 51.26	183	180	1.0 (0.12)
51.26 - 76.89	169	170	1.0 (0.10)
76.89 - 115.3	62	62	1.0 (0.15)
> 115.3	36	36	1.0 (0.18)

limit which, because of positive noise fluctuations, might have a measured flux above the limit. The total flux distribution has been simulated using the 90 cm source counts and angular size distribution reported by Owen et al. (2009). In particular, the sizes of sources have been randomly extracted from three different normal distributions with a mean value of 17, 7 and 4.5 arcsec for sources with a simulated flux of > 100 mJy, 10-100 mJy and < 10 mJy respectively (see Table 3 in Owen et al. 2009).

A total of 10 samples were simulated over an area of 3.14 square degree, i.e. equal to the area used to extract the 90 cm COSMOS catalog. According to the source counts distribution reported by Owen et al. (2009) (see their Table 8), we expect ~ 195 sources/deg² with a flux greater than 0.9 mJy, corresponding to ~ 610 sources for each simulated catalog of 3.14 square degrees. Considering all the samples, we simulated a total of 6115 sources, with a flux distribution as shown in Fig. 7.

For each simulated sample, the sources were randomly injected in the residual sky image (i.e. in the map with the real sources removed) and were recovered with fluxes measured using the same procedure adopted for the real sources (see Sect. 3.1). All the detected simulated sources from all the 10 simulated samples were then binned using the same flux intervals used in the source counts calculation. The results of our simulation are summarized in Table 2, where for each flux density bin we report the number of sources injected in the simulations, the number of sources detected using the same procedure adopted for the real data and the correction factor (C, with the relative standard deviation σ_C) to be applied to our observed source counts. Our simulations tell us that we are strongly incomplete below 3.0 mJy ($S/N \sim 6.0$) while at higher flux levels we are missing sources ($\sim 10\%$) only in the bin 3.0-4.5 mJy where a small correction factor of 1.1 must be applied. For fluxes greater than 4.5 mJy, there is no need to apply a correction.

4 324 MHZ SOURCE COUNTS

In order to reduce problems with possible spurious sources near the flux limit and effects of incompleteness (see `fab:simulation`) we constructed the 90 cm radio sources counts considering only the 171 sources with a flux density greater than 3.0 mJy, corresponding to a $S/N \gtrsim 6.0$. The 90 cm source counts are summarized in `fab:counts`, where, for each flux density bin, we report the mean flux density, the observed number of sources not corrected for the correction factor C, the differential source density dN/dS (in sr⁻¹ Jy⁻¹), the normalized differential counts $nS^{2.5}$ (in sr⁻¹ Jy^{1.5}) with

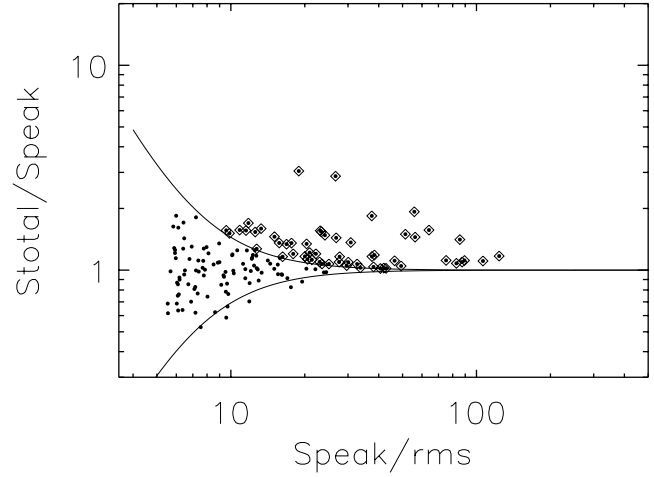


Figure 5. Ratio of the total flux S_T to the peak flux S_P as a function of the signal-to-noise ratio of the peak flux and the local rms for the 152 single component sources. The solid lines show the envelopes of the flux ratio distribution used to define resolved sources, indicated by open symbols in the panel.

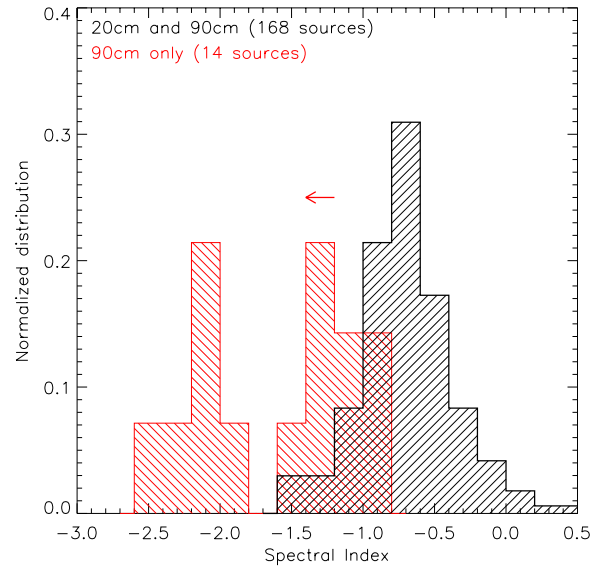


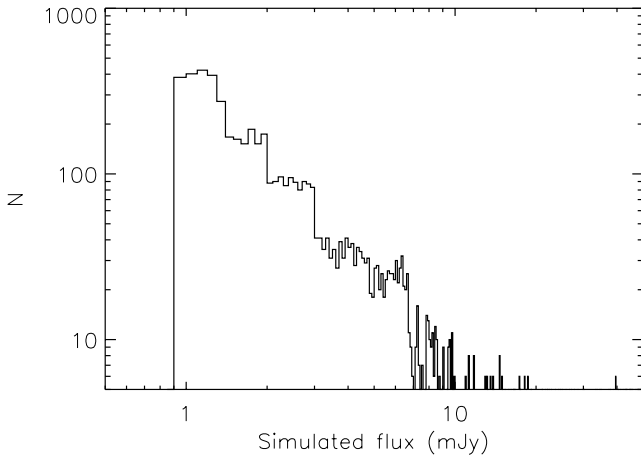
Figure 6. Distribution of 90-20 cm spectral indices for sources detected at both wavelengths (black), and those detected only at 90 cm (red). The latter yield upper limits to the spectral index (indicated by the arrow).

the estimated Poisson error (as $n^{1/2}S^{2.5}$) and the integrated counts $N(> S)$ (in deg⁻²).

The normalized differential counts $nS^{2.5}$ multiplied by the correction factor (C) reported in `fab:simulation`, are plotted in Fig. 8 where, for comparison, the differential source counts obtained from other 90 cm radio surveys are also plotted. As shown in Fig. 8 our counts are in very good agreement with previous surveys over the whole flux range sampled by our data ($\sim 3 - 250$ mJy). Unfortunately our 90 cm survey is not deep enough to confirm the flattening of the counts in the region below 3 mJy seen in other 90 cm surveys.

Table 3. The 90 cm Radio Source Counts for the COSMOS survey

S (mJy)	$\langle S \rangle$ (mJy)	N	dN/dS $\text{sr}^{-1} \text{Jy}^{-1}$	$nS^{2.5}$ $\text{sr}^{-1} \text{Jy}^{1.5}$	$N(> S)$ deg^{-2}
3.00 - 4.50	3.67	35	2.82×10^7	23.04 ± 3.91	56.91 ± 4.36
4.50 - 6.75	5.51	31	1.47×10^7	32.24 ± 5.97	44.05 ± 3.78
6.75 - 10.13	8.27	25	7.91×10^6	49.17 ± 9.83	33.94 ± 3.31
10.13 - 15.19	12.40	19	3.99×10^6	68.25 ± 15.66	25.81 ± 2.88
15.19 - 22.78	18.60	17	2.37×10^6	111.83 ± 27.12	19.66 ± 2.52
22.78 - 34.17	27.90	9	8.36×10^5	108.73 ± 36.34	14.18 ± 2.14
34.17 - 51.26	41.85	8	4.95×10^5	177.52 ± 62.76	11.28 ± 1.91
51.26 - 76.89	62.78	7	2.89×10^5	285.36 ± 107.85	8.70 ± 1.68
76.89 - 115.33	94.17	7	1.93×10^5	524.18 ± 198.12	6.44 ± 1.44
115.33 - 173.00	141.25	6	1.10×10^5	825.42 ± 336.98	4.19 ± 1.16
173.00 - 259.49	211.88	3	3.67×10^4	758.19 ± 437.74	2.26 ± 0.85

**Figure 7.** Flux distribution of the 6115 simulated sources used to test the completeness of our 90 cm sample

5 SOURCE PROPERTIES

In this section we analyze the redshift distribution, radio luminosities, and radio spectral indices of our 90 cm VLA-COSMOS sources. For this we use the most recent COSMOS photometric redshift catalog (version 1.8 with UltraVISTA data added where applicable; Ilbert et al. 2009, 2010; McCracken et al. 2012), the photometric redshift catalog for XMM-COSMOS sources presented by Salvato et al. (2009), and the most recent spectroscopic redshift catalog, comprising a compilation of all spectroscopic observations (public and internal) obtained to-date (zCOSMOS, Lilly et al. 2007, 2009, 2009; IMACS, Trump et al. 2007; MMT, Prescott et al. 2006; VUDS, Le Fevre et al. 2014.; Subaru/FOCAS, Nagao et al., priv. comm.; SDSS DR8, Aihara et al. (2011)).

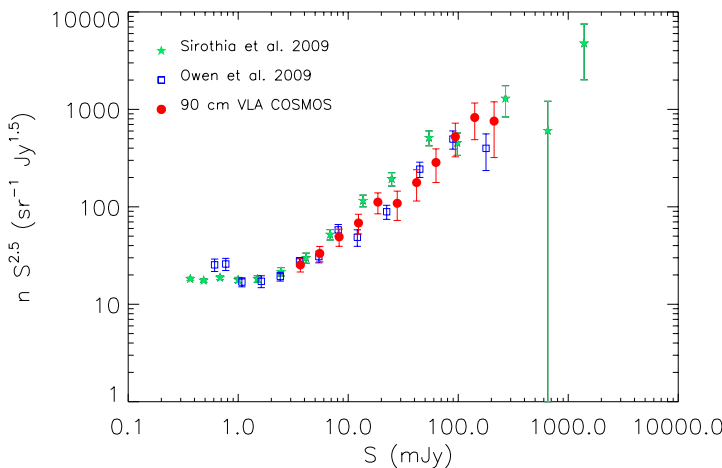
5.1 Redshift distribution and radio luminosities

We restrict our analysis to the area covered by the COSMOS 2 square degree survey. In the 324 MHz map we have identified a total of 182 sources ($S/N \geq 5.5$) over the 3.14 square degree area. Out of these 131 reside within the COSMOS 2 square degree area. Only 6 out of the 131 sources do not have a 20 cm VLA-COSMOS counterpart. Given that the 20 cm resolution (and thus the positional accuracy) is by about a factor of 5 better than that in our 90 cm map we hereafter use the 20 cm positions to match the 125 sources detected at 90 cm with other multi-wavelength catalogs. Following Sargent et al. (2010) we use a radius of $0.6''$ for the cross-correlation with optical and photometric redshift catalogs (see also Fig. 2 in Smolčić et al. 2008). Optical counterparts are identified for 115 out of 125 sources (i.e. 92%), however 4/115 are located in masked regions and thus no reliable photometry and photometric redshift could be determined for those (Ilbert et al. 2010). Matching the catalog with the full COSMOS spectroscopic catalog we identify 49 sources with a reliable spectroscopic redshift.

The cross-correlation of the optical sources with the XMM-COSMOS catalog has been done by Brusa et al. (2007). We identify 32 XMM sources in our sample of 115 90 cm sources with 20 cm radio and optical counterparts. 22 of these have reliable spectroscopic redshifts, and for the remainder we use photometric redshifts calculated by Salvato et al. (2009).

Hereafter we use spectroscopic redshifts where available, and photometric redshifts otherwise. The redshift distribution for the 111 sources detected at 90 cm is shown in Fig. 9. The redshift distribution peaks at $z \sim 1$, and shows an extended tail up to $z \sim 3$.

In Fig. 10 we show the 90 cm luminosity distribution of our

**Figure 8.** The 90 cm normalized differential source counts for our 90 cm VLA-COSMOS sources (red dots). Source counts at 90 cm from other surveys are also shown: N1 ELAIS field (Sirothia et al. 2009; filled green stars), *Spitzer* deep field 1046+59 (Owen et al. 2009; open blue square)

sources as a function of redshift. We also indicate the 5.5σ flux limit (assuming an average spectral index of -0.70), as well as the luminosity limits for various star forming (Milky Way, LIRG, ULIRG, HyLIRG assuming star formation rates of 4, 10, 100, $1000 M_{\odot} \text{ yr}^{-1}$, respectively) and AGN galaxies. For the latter we take a separation of $L_{90 \text{ cm}} = 3 \times 10^{25} \text{ W Hz}^{-1}$ between high- and low-power radio AGN (e.g. Kauffmann, Heckman & Best 2008). From the plot it is immediately obvious that the majority of our 90 cm sources are AGN. This is expected based on previous findings in radio surveys, and modeling of radio source populations (e.g. Wilman et al. 2008; Ballantyne 2009).

5.2 Spectral index as a function of redshift

The observed spectral index of radio sources has been shown to decrease as a function of redshift for sources with 1.4 GHz flux densities higher than 10 mJy (e.g. De Breuck et al. 2000). An explanation for this is related to a combination of the K-correction of a typically concave-shaped radio synchrotron spectrum ($\log F_{\nu} \propto \alpha \log \nu$ where α changes with frequency; see Miley & De Breuck 2008) and an increasing spectral curvature at high redshifts (mainly due to stronger inverse Compton losses in the denser cosmic microwave background at high redshifts; Krolik & Chen 1991). However, physical effects such as e.g. higher ambient density at higher redshift has to be invoked to explain the effect (see Miley & de Breuck 2008 for review). Thus, it has been suggested that high spectral indices of radio sources are an efficient proxy for identifying sources at high-redshifts. Although various efficient UV-NIR drop-out techniques have been identified to-date (e.g. Steidel et al. 1996), a purely radio-based high-redshift identifier may prove useful for currently conducted and planned future radio surveys (e.g. LOFAR all sky survey, WODAN and EMU) as these will have to rely on radio data only before the availability of next-generation UV-NIR sky surveys (e.g. LSST, Euclid).

To test whether a trend of steepening of spectral indices with increasing redshift exists or not we show the spectral index as a function of redshift for our sources detected at 90 and 20 cm with optical counterparts in Fig. 11. We find no clear evidence of spectral index steepening with redshift in our sample with a flux limit of ~ 2.75 mJy. This is consistent with the findings presented by Owen et al. (2009) who observed the Deep SWIRE field at 324.5 MHz down to an rms of $70 \mu\text{Jy/beam}$, and do not find a large population of ultra-steep spectrum sources down to this limit. Only one source in our sample has a spectral index steeper than $\alpha = -1.3$, the division usually used to identify high redshift source (e.g. De Breuck et al. 2000). Nevertheless, our data suggest that a selection of $\alpha < -1$ would select sources with $z \gtrsim 1$.

In the full 90 cm VLA-COSMOS catalog over 3.14 square degrees 182 sources were identified. Out of these 14 do not have counterparts at 20 cm (either in the 20 cm VLA-COSMOS or the FIRST surveys). Out of these 182 sources, in the previous sections we have analyzed 111 sources with 20 cm counterparts and reliable redshifts. Thus, 57 sources with 20 cm counterparts (=182-111-14) remain so-far unaccounted for. In Fig. 12 we show the spectral index distribution of the full 90 cm sample with 20 cm (VLA-COSMOS or FIRST) counterparts, as well as that of the 57 remaining sources. The distribution of the latter is very similar to that of the first (we find median spectral indices of -0.70 and -0.74 for the full sample, and the subsample, respectively). This suggests similar physical properties of the sources in the two samples. Furthermore, applying a cut of $\alpha < -1$ to the subsample of 57 sources

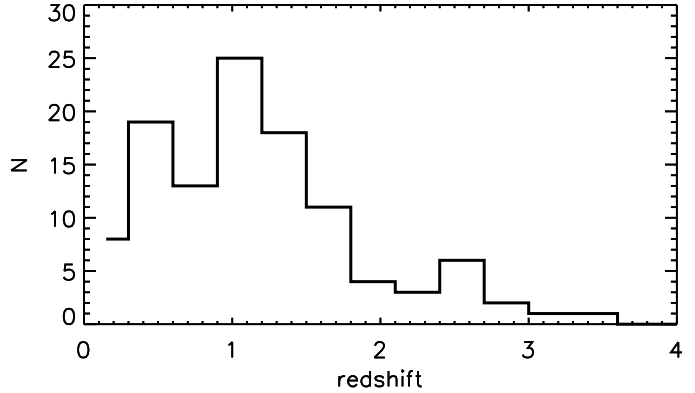


Figure 9. Redshift distribution of the VLA-COSMOS 90 cm sources with NUV-NIR counterparts, and reliable photometric or spectroscopic redshifts.

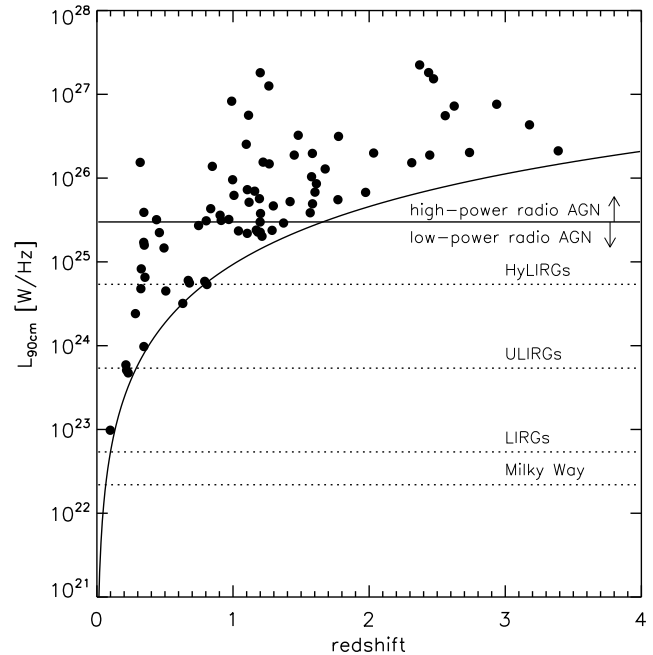


Figure 10. 90 cm luminosity as a function of redshift for our 324 MHz detected sources. The curve shows the 5.5σ limit of our 90 cm data (assuming a spectral index of 0.7), and the horizontal lines indicate the locations in this diagram of various types of galaxies (labeled in the panel). Note that at the 90 cm flux limit we predominantly identify AGN galaxies.

suggests that 7 of these can be identified without other information to be at high redshift, i.e. $z \gtrsim 1$.

6 SUMMARY

We have presented a 90 cm VLA map of the COSMOS field, comprising a circular area of 3.14 square degrees at $6.0'' \times 5.3''$ angular resolution with an average rms of 0.5 mJy/beam . The ex-

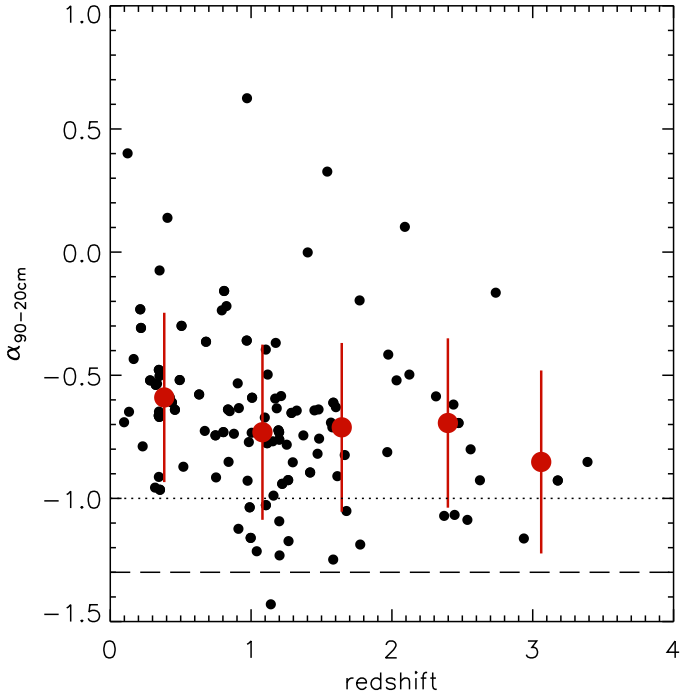


Figure 11. 90-20 cm spectral index vs. redshift (spectroscopic where available, otherwise photometric) for our sources detected at 90 cm. The median and root-mean-square scatter of the distribution are also shown (filled dots and vertical error-bars, respectively). The horizontal lines indicate spectral indices of -1 and -1.3.

tracted catalog contains 182 sources, 30 of which consist of multiple components. Using Monte Carlo artificial source simulations we have derived the completeness correction for the catalog. Our source counts agree very well with those from previous studies, verifying the validity of the catalog. As expected based on previous findings in radio surveys, and modeling of radio source populations (e.g. Wilman et al. 2008; Ballantyne 2009) our sample is AGN dominated, as inferred based on 90 cm radio luminosity considerations.

Combining the 90 cm with our 20 cm VLA-COSMOS data we infer a median 90-20 cm spectral index of -0.70, with an interquartile range of -0.90 to -0.53. This is consistent with values found at 90 vs. 20 cm wavelengths (Owen et al. 2009), as well as that typically found for radio sources at high (GHz) radio frequencies (e.g. Kimball & Ivezić 2008).

Making use of the COSMOS photometric and spectroscopic redshifts of our 90 cm sources we find no strong evidence for steepening of the spectral index with redshift. The sources in our sample with spectral indices steeper than -1 all lie at $z \gtrsim 1$, in agreement with the idea that ultra-steep-spectrum radio sources may trace intermediate-redshift galaxies ($z \gtrsim 1$).

ACKNOWLEDGEMENT

VS acknowledges the European Unions Seventh Framework program grant agreement 333654 (CIG, 'AGN feedback') and the Australian Group of Eight European Fellowship 2013. AK acknowledges support by the Collaborative Research Council 956, sub-project A1, funded by the Deutsche Forschungsgemeinschaft

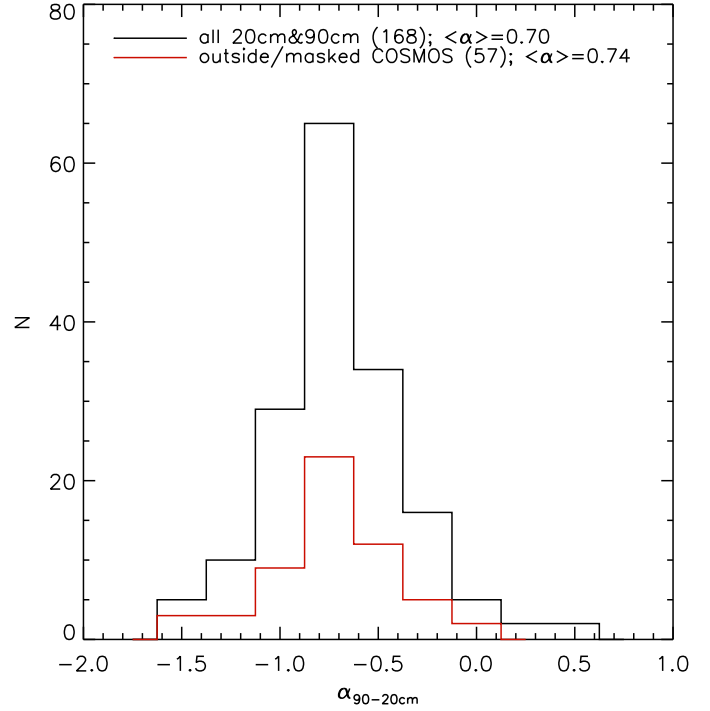


Figure 12. 90-20 cm spectral index distribution for all sources in the 90 cm VLA-COSMOS catalog with 20 cm (VLA-COSMOS Deep or FIRST) counterparts (black line), and the subsample of sources either outside the COSMOS 2sq.deg. area or those within the COSMOS 2 square degree area, but without optical counterparts or reliable redshifts (red line). The similar spectral index distribution suggests similar physical properties of the two samples.

(DFG). The National Radio Astronomy Observatory is a facility of the National Science Foundation operated under cooperative agreement by Associated Universities, Inc.

REFERENCES

- Aihara H. et al., 2011, *ApJS*, 193, 29
- Ballantyne D. R., 2009, *ApJ*, 698, 1033
- Best P. N., Heckman T. M., 2012, *MNRAS*, 421, 1569
- Birzan L., McNamara B. R., Nulsen P. E. J., Carilli C. L., Wise M. W., 2008, *ApJ*, 686, 859
- Birzan L., Rafferty D. A., McNamara B. R., Wise M. W., Nulsen P. E. J., 2004, *ApJ*, 607, 800
- Bondi M. et al., 2007, *A&A*, 463, 519
- Bondi M. et al., 2003, *A&A*, 403, 857
- Bower R. G., Benson A. J., Malbon R., Helly J. C., Frenk C. S., Baugh C. M., Cole S., Lacey C. G., 2006, *MNRAS*, 370, 645
- Brusa M. et al., 2007, *ApJS*, 172, 353
- Capak P. et al., 2007, *ApJS*, 172, 99
- Condon J. J., 1997, *PASP*, 109, 166
- Croton D. J. et al., 2006, *MNRAS*, 365, 11
- De Breuck C., Tang Y., de Bruyn A. G., Röttgering H., van Breugel W., 2002, *A&A*, 394, 59
- De Breuck C., van Breugel W., Röttgering H. J. A., Miley G., 2000, *A&AS*, 143, 303
- Elvis M. et al., 2009, *ApJS*, 184, 158

- Evans D. A., Worrall D. M., Hardcastle M. J., Kraft R. P., Birkinshaw M., 2006, *ApJ*, 642, 96
- Greisen E. W., 1990, in *Acquisition, Processing and Archiving of Astronomical Images*, Longo G., Sedmak G., eds., pp. 125–142
- Hardcastle M. J., Evans D. A., Croston J. H., 2007, *MNRAS*, 376, 1849
- Hasinger G. et al., 2007, *ApJS*, 172, 29
- Ho L. C., 2005, *Astrophys. Space Sci.*, 300, 219
- Hopkins A. M., Afonso J., Chan B., Cram L. E., Georgakakis A., Mobasher B., 2003, *AJ*, 125, 465
- Ilbert O. et al., 2009, *ApJ*, 690, 1236
- Ilbert O. et al., 2010, *ApJ*, 709, 644
- Jelić V., Smolčić V., Finoguenov A., Tanaka M., Civano F., Schinnerer E., Cappelluti N., Koekemoer A., 2012, *MNRAS*, 423, 2753
- Johnston S. et al., 2007, *Publications of the Astronomical Society of Australia*, 24, 174
- Kauffmann G., Heckman T. M., Best P. N., 2008, *MNRAS*, 384, 953
- Kimball A. E., Ivezić Ž., 2008, *AJ*, 136, 684
- Koekemoer A. M. et al., 2007, *ApJS*, 172, 196
- Krolik J. H., Chen W., 1991, *AJ*, 102, 1659
- Le Fevre O. et al., 2014, *ArXiv e-prints*
- Lilly S. J. et al., 2009, *ApJS*, 184, 218
- Lilly S. J. et al., 2007, *ApJS*, 172, 70
- McCracken H. J. et al., 2012, *A&A*, 544, A156
- Miley G., De Breuck C., 2008, *A&ARv*, 15, 67
- Mobasher B. et al., 2007, *ApJS*, 172, 117
- Norris R. P. et al., 2011, *Publications of the Astronomical Society of Australia*, 28, 215
- Oklopčić A. et al., 2010, *ApJ*, 713, 484
- Owen F. N., Morrison G. E., Klimek M. D., Greisen E. W., 2009, *AJ*, 137, 4846
- Prescott M. K. M., Impey C. D., Cool R. J., Scoville N. Z., 2006, *ApJ*, 644, 100
- Salvato M. et al., 2009, *ApJ*, 690, 1250
- Sanders D. B. et al., 2007, *ApJS*, 172, 86
- Sargent M. T. et al., 2010, *ApJS*, 186, 341
- Schinnerer E. et al., 2004, *AJ*, 128, 1974
- Schinnerer E. et al., 2010, *ApJS*, 188, 384
- Schinnerer E. et al., 2007, *ApJS*, 172, 46
- Scoville N. et al., 2007, *ApJS*, 172, 1
- Sijacki D., Springel V., 2006, *MNRAS*, 366, 397
- Sirothia S. K., Dennefeld M., Saikia D. J., Dole H., Riquebourg F., Roland J., 2009, *MNRAS*, 395, 269
- Smolčić V., 2009, *ApJL*, 699, L43
- Smolčić V. et al., 2008, *ApJS*, 177, 14
- Smolčić V. et al., 2009, *ApJ*, 696, 24
- Steidel C. C., Giavalisco M., Pettini M., Dickinson M., Adelberger K. L., 1996, *ApJL*, 462, L17
- Taniguchi Y. et al., 2007, *ApJS*, 172, 9
- Tasse C., Röttgering H. J. A., Best P. N., Cohen A. S., Pierre M., Wilman R., 2007, *A&A*, 471, 1105
- Trump J. R. et al., 2007, *ApJS*, 172, 383
- White R. L., Becker R. H., Helfand D. J., Gregg M. D., 1997, *ApJ*, 475, 479
- Wilman R. J. et al., 2008, *MNRAS*, 388, 1335